Microscopy and Microanalysis (2021), **27**, 1328–1337
doi:10.1017/S1431927621012745

Microscopy AND Microanalysis

Original Article

Detection and Localization of Eu on Biosilica by Analytical Scanning Electron Microscopy

Ellen Hieckmann[1*a], Kaitlin K. K. Kammerlander[2,a], Lydia Köhler[2,a], Laura Neumann[1,a], Stefan Saager[3], Nico Albanis[1,b], Thomas Hutsch[4], Frank Seifert[5,b] and Eike Brunner[2]

[1]Faculty of Physics, Institute of Applied Physics, TU Dresden, Helmholtzstraße 10, Dresden, Saxony 01069, Germany; [2]Faculty of Chemistry and Food Chemistry, Chair of Bioanalytical Chemistry, TU Dresden, Dresden, Saxony 01069, Germany; [3]Fraunhofer Institute for Organic Electronics, Electron Beam and Plasma Technology FEP, Dresden, Saxony 01277, Germany; [4]Fraunhofer Institute for Manufacturing Technology and Advanced Materials IFAM, Branch Lab Dresden, Dresden, Saxony 01277, Germany and [5]Faculty of Physics, Institute of Nuclear and Particle Physics, TU Dresden, Dresden, Saxony 01069, Germany

Abstract

Algae like diatoms are widely studied as a means to remediate anthropogenically contaminated sites. In the present study, CL (cathodoluminescence) and EDX (energy-dispersive X-ray) spectroscopy in an SEM (scanning electron microscope) were optimized for the detection of Eu(III) sorbed on diatom biosilica. The required stability of biosilica under a focused electron beam was extensively investigated. Using experimentally determined data of thermal properties, the temperature increase within biosilica exposed to an electron beam was simulated by finite element calculations based on results from Monte Carlo simulations of electron scattering. Complementary thermogravimetric studies substantiated a chemical stability of biosilica in a wide temperature range, confirming its suitability for long-lasting SEM investigations. In subsequent EDX measurements, characteristic Eu lines were detected. Eu was found to preferentially accumulate and aggregate on silica fragments. CL spectra were obtained for the Eu(III) reference material, $EuCl_3$. For Eu-loaded biosilica, even parts without detectable Eu signal in the EDX spectra show significant Eu(III) signals in the CL spectra. This highlights the sensitivity of CL in studying *f*-element sorption. CL data showed that Eu(III) was distributed on the entire surface. In conclusion, this work demonstrates the merit of CL and EDX methods for sorption studies on biogenic materials.

Key words: cathodoluminescence, diatoms, europium, Monte Carlo simulation, SEM

(Received 30 January 2021; revised 11 July 2021; accepted 30 August 2021)

Introduction

The removal of lanthanides and actinides from the environment is of utmost importance. On the one hand, anthropogenically contaminated sites need to be remediated, thus restoring the original state of natural habitats. On the other hand, a fundamental understanding of the interactions of *f*-elements with naturally occurring substrates helps to evaluate their mobility in the environment and interactions with therein occurring substances and organisms (Götzke et al., 2019).

A typical removal strategy is to accumulate the target substances by a substrate like a sorbent material. Thereby, "green" sorbents are preferable, i.e., nontoxic materials that can be gained energy-efficiently and without harmful reagents and by-products. Biogenic materials often fulfill these requirements better than synthetic materials (Matheickal et al., 1997; Xiao & Howard Huang, 2009; Ansone et al., 2014).

A widely used filter and sorbent material is diatomite or diatomaceous earth (DE) (Wang et al., 2014). This material consists largely of sedimented, fossilized siliceous diatom cell walls (Kogel et al., 2006). Diatom cell walls, the so-called frustules, stand out from other unicellular algae due to their uniquely patterned, porous silica structure (Round et al., 1990; Mann, 1999). These properties render frustules attractive as sorbents from the materials science point of view. However, diatomite also contains mineral impurities, depending on the mining site. Silica in diatomite is also aged: compared to its initial state, it has lost a large amount of silanol groups (Si–OH), which were transformed into siloxane (Si–O–Si) by water elimination (Loucaides et al., 2010). SiOH groups are, however, favorable adsorption sites for positively charged ions because they partially dissociate into SiO^- and H^+ (Iler, 1979).

"Fresh" diatom frustules, i.e., biosilica directly gained from living diatoms, are thus to be favored. Diatom cultivation under controlled conditions for specific applications also provides the opportunity for tailoring the cells *in vivo* (Gutu et al., 2005; Lang et al., 2013; Köhler et al., 2017). Genetic modifications or variations of growth conditions are possible, e.g., by the addition

***Corresponding author:** Ellen Hieckmann, E-mail: ellen.hieckmann@tu-dresden.de
[a]These authors contributed equally.
[b]Affiliation is former affiliation, now employed in the private/state sector.

Cite this article: Hieckmann E, Kammerlander KKK, Köhler L, Neumann L, Saager S, Albanis N, Hutsch T, Seifert F, Brunner E (2021) Detection and Localization of Eu on Biosilica by Analytical Scanning Electron Microscopy. *Microsc Microanal* **27**, 1328–1337. doi:10.1017/S1431927621012745

of substances that are taken up and potentially incorporated into the biosilica. Furthermore, fresh frustules usually exhibit a higher specific surface area. Diatomite comprises only heavily silicified, massive cell walls because filigree structures dissolve faster after the removal of the organic coating following cell death (Bidle & Azam, 1999; Kooistra et al., 2007). Consequently, both fresh and aged diatom biosilica are evaluated as filter or sorbent materials for *f*-elements (Kammerlander et al., 2021). For fundamental research, fresh biosilica is also advantageous because it represents a comparably well-defined material. It thus constitutes a suitible substance for the modeling of sorptive interactions in the frame of radiotoxic remediation.

Europium(III) can be used as a convenient, nontoxic analog for chemically similar trivalent, radioactive actinides (Stumpf et al., 2007). To analyze the interactions of Eu(III) with its environment, a wide range of analytical methods is employed (Götzke et al., 2019). For example, plant, rock, and soil contents or sorbent loadings are quantified by element analyses like ICP-AES (inductively coupled plasma atomic emission spectroscopy) (Alexandre et al., 2015) and MS (mass spectrometry) (Yamamoto et al., 2010). X-ray diffraction methods, which are widely applied in the case of minerals or other crystalline sorbents (Santos-Beltran et al., 2018), are unsuitable for amorphous phases like diatom biosilica. Some of the typical molecular spectroscopy methods like standard Raman spectroscopy are not sufficiently sensitive for small amounts of adsorbed analytes.

In contrast, fluorescence spectroscopy provides an extraordinary sensitivity. For the respective methods, Eu is a convenient probe due to its remarkable luminescence properties. Information about the complexation strength, the number of individual species as well as the chemical environment can be extracted from luminescence data (Binnemans, 2015). In particular, TRLFS (time-resolved laser-induced fluorescence spectroscopy) is a widespread method to characterize Eu bound to various organic substances and minerals (NordÉn et al., 1992; Mathur et al., 2006; Stumpf et al., 2007). However, standard TRLFS—like the analytical methods mentioned above—cannot determine the spatial distribution of the sorbate on the sorbent material. The recently developed μTRLFS addresses this issue. While it is a highly valuable tool for mineral studies in the context of permanent disposal sites, its laser excitation spot with a diameter of about 30 μm limits its use in the analysis of microalgae samples (Molodtsov et al., 2019).

The high resolution necessary to characterize micro- and nanopatterned samples can be provided by CL (cathodoluminescence) investigations in an SEM (scanning electron microscope). For example, sub-20-nm nanoparticles consisting of lanthanide-doped $NaGdF_4$ and $NaYF_4$ were successfully resolved by CL-SEM (Prigozhin et al., 2019). CL spectroscopy and imaging are often used to study the band edge emission and to characterize zero-dimensional as well as extended defects in various different samples such as semiconductors, minerals, and rocks (Gaft et al., 2005; Coenen & Haegel, 2017). For trivalent rare earth elements, the radiative transitions of the 4*f*-electrons can be excited by the electron beam and result in characteristic, narrow lines, which are especially useful in this context (Binnemans, 2015).

The aim of the current investigation is the analysis of the local distribution and complexation of luminescent Eu(III) loaded on diatom frustules. Therefore, imaging and spectroscopic analytical methods in an SEM are optimized and applied. The sensitive and spatially resolved CL method is complemented by EDX (energy-dispersive X-ray) spectroscopy, including elemental imaging. The EDX method exhibits a similar spatial resolution (Imeson, 1982), is less prone to spectral interferences compared to CL spectroscopy, and has been successfully applied for the analysis of metal-loaded plant cell walls in the past (Fritz, 2007). However, acquiring EDX maps of sorbates with low concentrations is very time-consuming. In addition, EDX spectroscopy provides no information about the Eu complexation. Using these complementary methods with high sensitivity and resolution, the distribution of Eu species over the frustules can be elucidated. For the evaluation of the CL spectra of the Eu-loaded biosilica, the contribution of the single components is evaluated by measurements of pure reference materials: Eu salt and biosilica without Eu.

The chosen analytical methods require the stability and durability of the samples under electron beam irradiation. Though diatoms are frequently studied by SEM and EDX investigations, stability issues are rarely evaluated. The current paper therefore addresses the energy impact and resulting thermally induced deformation of the frustules' structure. The temperature increase was modeled by finite element calculations, taking into account results from the Monte Carlo simulation of electron scattering in the biosilica. Because thermal properties of the material had to be known for the temperature calculations, differential scanning calorimetry (DSC) was used to determine the heat capacity. Furthermore, the flash method was applied to characterize the thermal conductivity of the fresh diatom silica as well as commercially available diatomite and silica gel as reference materials. Additionally, the materials were analyzed with DTA/TG-MS (differential thermal analysis/thermogravimetry coupled with MS) to study their thermal stability and potential gaseous decomposition products.

Materials and Methods

Cultivation of the Diatoms

Diatoms were cultivated in RUMED 1301 light thermostats (Rubarth Apparate) at 21°C with a 12/12 h light (1,000 lx)/dark illumination cycle. As growth vessels, 20 L polyethylene carboys (Thermo Fisher Scientific) were used. The culture medium was sterile filtered artificial seawater according to the recipe of the North East Pacific Culture Collection (Harrison et al., 1980). The strain of *Stephanopyxis turris* (*S.t.*) had been collected by the Sumper group of the Universität Regensburg (Regensburg, Germany) from the North Sea in 2004. Its identity was genetically confirmed in 2017 (Pytlik et al., 2017). After inoculation, the cultures grew for about 1–2 months until the silicon concentration in the growth medium was depleted below 5 μmol/L. This was confirmed by the colorimetric molybdenum blue method according to Iler (Iler, 1979). Consequently, cells were harvested by centrifugation using a Hereaus Megafuge with 4,000 rpm.

Cleaning and Eu Loading of the Diatom Biosilica

The brown-green, "native" cell pellets were cleaned by a treatment with a lysis buffer. The cells were suspended in 20 mL lysis buffer, a solution of 20 g/L sodium dodecyl sulfate (SDS, Merck) and 37 g/L sodium ethylene diamine tetraacetic acid (Na_2EDTA, Grüssing) adjusted to pH 8. The mixture was heated to 95°C for 10 min, subsequently cooled, and centrifuged with 4,000 rpm. The supernatant was discarded. The pellet was subjected to two to six further iterations of the lysis buffer treatment until the supernatant was nearly colorless. Subsequently, the cleaned cells were washed five times with ultrapure water and freeze-dried at −55°C and

https://doi.org/10.1017/S1431927621012745 Published online by Cambridge University Press

0.47 mbar in a 1-4 LSC basic device (Christ Alpha). The resulting powder was calcined in a Carbolite AAF 1100 muffle furnace at 550°C for 10 h under a static air atmosphere to remove residual organic substances from the silica.

In the course of the Eu sorption experiments, 10 mg of the biosilica was suspended in 10 mL of a solution of 10^{-3} mol/L Eu(III) in ultrapure water with 0.1 mol/L $NaClO_4$ as background electrolyte. The pH was adjusted to pH 5 with $HClO_4$ and NaOH. The suspension was shaken for 3 days and, afterward, centrifuged at 4,000 rpm. The supernatant was separated from the diatom sorbate, which was subsequently dried under air atmosphere.

Mounting of SEM Samples

Several milligrams of the dried diatom material were resuspended and transferred to a clean aluminum stub. Likewise, stubs with the procured reference material silica gel 60 (0.015–0.040 mm, Merck) were prepared. To avoid electrostatic charging, the dried samples were sputtered with gold using a Q150R sputter coater (Quorum Technologies), resulting in a 5 nm thick gold coating.

Imaging, EDX, CL, and Electron Diffraction in the SEM

Imaging, EDX, as well as CL investigations were carried out at room temperature and a pressure of about 10^{-6} mbar using a Zeiss Ultra55 SEM with a field emission gun. The current I_B of the primary electron beam on the sample surface was measured by an internal sample current detector. An Everhart–Thornley detector and an Inlens detector were deployed for secondary electron imaging of the diatoms. The electron beam moves with a rate of about 44 mm/min (for imaging) to $1.5 \cdot 10^4$ mm/min (for spectra in area scan mode). This corresponds to beam dwell times of $1.4 \cdot 10^{-3}$ and $4.0 \cdot 10^{-6}$ s/µm, respectively.

The elemental composition was determined by the microanalysis system Quantax from Bruker AXS with an XFlash detector 4010 and the software Esprit 1.9.2. For a bulk SiO_2 sample, the depth Z, at which the detectable X-ray radiation of Eu L-lines is generated by electrons at the applied acceleration voltage U_B of 13 kV, is about 2 µm (cf. Supplementary material section 1). It is, thus, significantly greater than the diameter of the electron beam on the sample surface (spot size approximates to 2 nm).

During SEM imaging for stability investigations, parameters corresponding to subsequent CL measurements were chosen for the electron beam ($U_B = 10$ kV and $I_B = 27.5$ nA). Under these conditions, the image pixel size of 65 nm is smaller than the penetration depth R of primary electrons, which is about 1 µm (cf. Supplementary material section 1). Assuming that in a bulk sample, the penetration depth R corresponds approximately to the diameter of the excitation volume, where the CL light registered by the CL system originates, the spatial resolution of CL measurements as defined by Yacobi and Holt (1990) is low in relation to image resolution and comparable to that of EDX investigations.

The spectral CL measurements were performed with a system that consists essentially of a parabolic mirror segment, a Czerny-Turner monochromator, an on-axis mounted Peltier-cooled CCD camera S7031-1006 from Hamamatsu (back-illuminated, 1,024 × 64 pixels) for the wavelength range between 200 and 1,200 nm, and a Hamamatsu photomultiplier R3896 for the range between 200 and 900 nm. A blazed grating with 300 lines/mm and blaze wavelength at 500 nm was applied for the acquisition of the CL spectra with the operation software PSI line. The instrumental broadening of the spectral lines is 17 nm/mm by the aperture size of the monochromator.

Due to the shadowing of X-rays by the parabolic mirror segment during CL investigations, EDX and CL measurements could not be performed simultaneously on one sample. Normally, EDX analysis was carried out after the CL tests.

The crystallinity of the samples was probed by electron backscatter diffraction (EBSD), using an HKL Nordlys detector system and the Channel5 evaluation software.

Thermal Analysis

To determine the specific heat capacity, DSC measurements were conducted with a NETZSCH DSC 204 F1 Phoenix calorimeter. Sapphire specimens (thickness 0.5/1.0 mm) were used as reference materials. The investigated temperature ranges from 0 to 420°C, applying a heating rate of 10 K/min under argon atmosphere. An aluminum pan with a pierced lid was used as a sample holder for silica samples including DE (Merck) as a silica reference. Additionally, DTA/TG-MS results were obtained by a NETZSCH STA 449 F3 Jupiter analyzer in a temperature range of 26–1,050°C. These measurements were also conducted with a heating rate of 10 K/min under argon atmosphere. Samples were placed in alumina crucibles. Thermal conductivity analyses were carried out with a NETZSCH LFA 447 NanoFlash device using the flash method. A measuring cell with flash-transparent windows was applied, which was developed by Pohlmann et al. (2013). The thermal conductivity was calculated by the multiplication of thermal diffusivity, specific heat and mass density.

Monte Carlo Simulations and Finite Element Method

To determine the spatial distribution of the heat energy impact of primary electrons into bulk silica material, the free Monte Carlo simulation software CASINO Version 2.4.8.1 was used (Drouin et al., 2007; Demers et al., 2011). Based on these results, the temperature distribution in the diatom frustule structure was calculated from a three-dimensional non-linear heat conduction equation (cf. Supplementary material section 2, Supplementary eq. 1). This equation was numerically solved by the finite element method (FEM) with the Software Comsol Multiphysics ® Version 5.6 utilizing the Heat Transfer Module (Comsol, 2020). A detailed description of the simulation procedure can be found in a former publication (Saager, 2016). For the diatom sample and its cell wall, which has a honeycomb-like structure comprised of chamber-like pores (shaped like prisms with a hexagonal base), the following parameters were used: mass density of 2.36 g/cm³, sieve plate (base of the chamber-like pore) thickness of 60 nm, chamber wall (perpendicular to the sieve plate) height of 0.5 µm and thickness of 80 nm, and hexagon side length of 2 µm.

Results and Discussion

Stability Issues in SEM Imaging of Diatom Frustules

It is known from the literature (Stevens-Kalceff, 2013; Bhowmick et al., 2015) that the properties of silica can be modified by the electron beam in an SEM. To assess the stability of silicified microorganisms—especially diatom biosilica—under the exposure of the scanning electron beam, morphological changes were investigated here.

https://doi.org/10.1017/S1431927621012745 Published online by Cambridge University Press

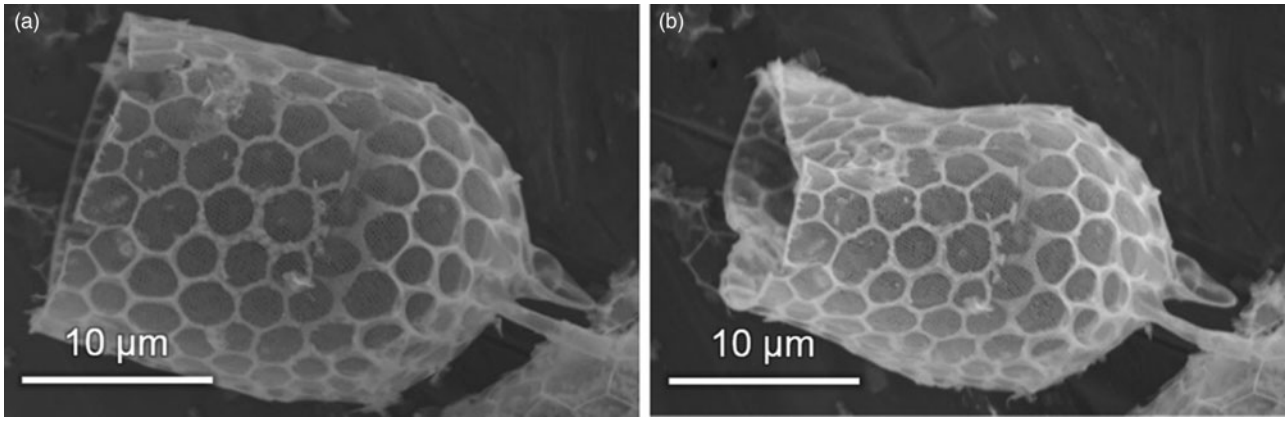

Fig. 1. SEM image of a typical valve extracted from the diatom species *S.t.* at the beginning (**a**) and after 150 min of electron irradiation (**b**).

Figure 1a shows a representative valve from the species *S.t.* The entire diatom frustule consists of two valves connected to each other by girdle bands. When stabilizing organic constituents are removed from the biosilica during the extraction and cleaning process, the different parts of the frustule are usually disconnected. The depicted valve has kept its initial half-shell shape through cell lysis and calcination.

As illustrated in Figure 1b, the morphology of the cell wall changes considerably after 150 min of electron irradiation time. All observed frustules show a similar behavior, regardless of the presence or the absence of Eu(III). Probably, the frustule shape changes due to the heat energy input caused by the inelastic scattering of the primary electrons. The resulting temperature gradients during irradiation could induce mechanical stress, structure instability, and finally frustule deformation. Furthermore, a charging effect may be conceivable in principal: the primary electron beam could induce a locally accumulating charge, leading to increasing mechanical stress due to electrostatic forces. However, in contrast to conducted SEM analyses of uncoated frustules, no signs of irradiation-induced electrical charging, like charge contrast or image drift, were observed in the present samples. Thus, significant effects due to charging are improbable.

Deformations might also be assisted by a mass loss at higher temperatures. For the evaluation of these influences and possible chemical transformations, the local temperature increase in the diatom frustule has to be assessed. To this end, several thermal properties must be determined.

Thermal Analysis

Values of the specific heat capacity and thermal diffusivity of the silica materials were determined via simultaneous thermal analysis (STA) in DTA/TG-MS mode and the flash method, respectively. Thus, the thermal stability of the biosilica was evaluated and gas molecules formed during thermal decomposition could be detected.

In the present study, calcined diatom frustules were used for Eu sorption experiments. The calcination is part of the sample pretreatment and is crucial for thermal stability. It reduces the mass of biosilica by about 40%, which is in accordance with other studies reporting a mass loss of 20% (Meradi et al., 2016) to 50% (Jiang et al., 2014) for the calcination of cultivated and chemically pretreated diatom cells. For untreated diatomite, lower losses of about 10% are reported (Fuya et al., 1995; Nowak et al., 2019).

In Figure 2, TG and DTA curves as well as corresponding MS signals from gaseous products that escape during heating from *S.t.* biosilica are depicted. At temperatures below 40°C, flushing the porous samples with argon can lead to buoyancy effects, resulting in a perceived mass loss. At temperatures above 60°C, three effects can be distinguished. Beginning from 100 to 300°C, a smooth exothermic effect can be observed in the DTA curves with the simultaneous release of fragments of N_2 (m/z 28) and O_2 (m/z 32). This signal is probably due to the desorption of atmospheric air. A strong exothermic effect occurs at 400 to 700°C. This coincides with a sharp release of fragments of N_2 (m/z 28) and O_2 (m/z 32) at about 520°C. Possible fragments of CO_2 (m/z 44) could be surmised due to the slightly elevated baseline in the region from 400 to 650°C. The signal-to-noise ratio suggests that the potential CO_2 release is negligible. Additionally, fragments of SO (m/z 48) and SO_2 (m/z 64) can be identified between 500 and 700°C. Above 850–900°C, the TG signal indicates the onset of a mass loss caused by an increasing release of SO (m/z 48) and SO_2 (m/z 64) fragments. These signals can be attributed to remnants of organic matter, mainly sulfate esters of saccharides (Tesson et al., 2009), and residues of the SDS treatment. At a temperature near the maximum of 1,000°C, another onset of N_2/O_2 release can be observed in the graphs. Such high temperatures over 925°C can damage the internal pore structure and, thus, release trapped air (König et al., 2020).

No significant water signals due to pore water removal or condensation of the surficial silanol groups to siloxanes (Meradi et al., 2016) can be observed in both DTA/TG and MS graphs. To a certain degree, siloxane groups could have already formed during the thermal pretreatment of the biosilica at 550°C. This temperature was chosen to remove organic material while retaining some isolated silanol groups, as was shown in former studies (Nawrocki, 1997; Yuan et al., 2004), and for reasons of comparability to preceding works (Machill et al., 2013; Köhler et al., 2017). While calcination conditions may vary significantly for different types of algae (Liu, 2019), these results show that this pretreatment sufficiently removes almost all organic material and provides a thermally stable biogenic silica material for further application as a sorbent.

Apart from the perceived mass loss at temperatures below 100°C, the low total mass loss of about 1% suggests that calcined *S.t.* biosilica is relatively stable under conditions up to ca. 900°C in an inert atmosphere.

In Figure 3, the temperature dependency of the specific heat capacity c_p of several thermally pretreated silica materials are

https://doi.org/10.1017/S1431927621012745 Published online by Cambridge University Press

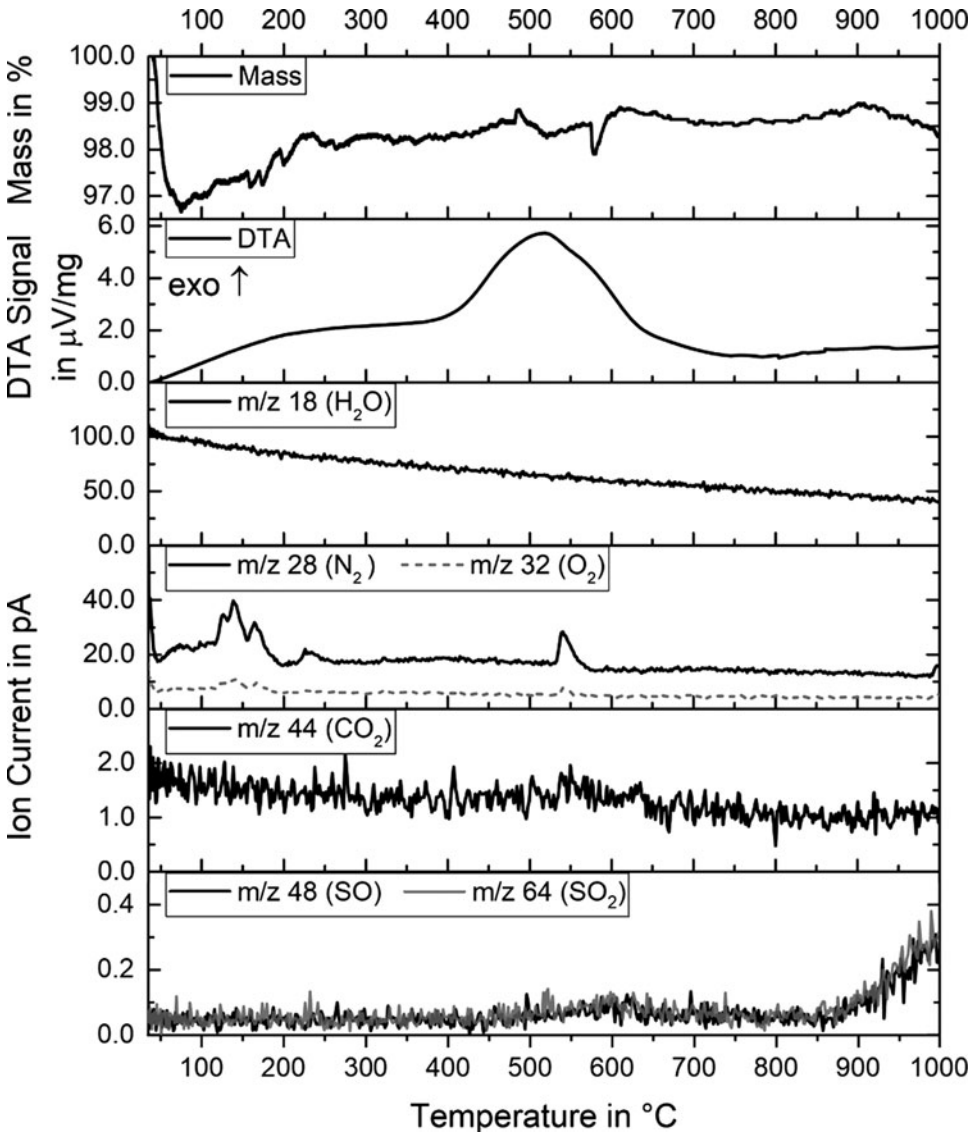

Fig. 2. Mass (TG), DTA, and MS curves for *S.t.* biosilica. MS results of m/z 18 (H_2O), 28 and 32 (N_2 and O_2; air), 44 (CO_2), and 48 as well as 64 (SO and SO_2) during thermal analysis.

compared. The percentage of non-siliceous impurities in the frustules of *S.t.* lies in between the pure, artificial silica gel and the biogenic DE, which contains various mineral impurities. The c_p values of *S.t.* show the first maximum of about 1.2 J/g K at around 90°C, similar to silica gel. The c_p maximum of DE at about 160°C is only slightly indicated in the *S.t.* graphs. This is probably due to the release of air as seen in Figure 2, which may also cause the local, low-intensity maximum at ca. 250°C.

The supporting points for a linear interpolation of the c_p-T curve in the subsequent simulation of the temperature distribution in the sample due to electron irradiation are marked by black squares in Figure 3. An experimental value for the thermal conductivity λ of the diatomaceous material is only available for room temperature. For the temperature simulation explained in the next section, it was thus assumed that biosilica shows the same increase in thermal conductivity per temperature increase as spectrosil (cf. Supplementary Fig. 1). For this material, detailed data are provided in the literature (Heraeus, 2019).

Modeling of the Temperature Increase in the Frustule under the Electron Beam

With the material data from the thermal analyses and with the results from the Monte Carlo simulation (cf. Supplementary Fig. 2), the temperature distribution in a diatom valve was modeled by FEM calculations for an idle electron beam with $U_B = 10$ kV and $I_B = 27.5$ nA. The resulting temperature distribution is shown in Figure 4. Thereby, the filigree diatom structure is taken into account. The honeycomb-like pore structure plays a significant role, as shown by comparison to simulations with a bulk silica material. The limited possible interaction volume decreases the heat power input through the electron beam. In contrast, the maximum temperature can increase, as the small volume impedes the heat conduction.

In the case of a point-like excitation (equivalent to an infinite irradiation time, whereby thermal equilibrium is reached after some milliseconds) as shown in Figure 4, a maximum local temperature increase of about 300 K is calculated in a frustule region

https://doi.org/10.1017/S1431927621012745 Published online by Cambridge University Press

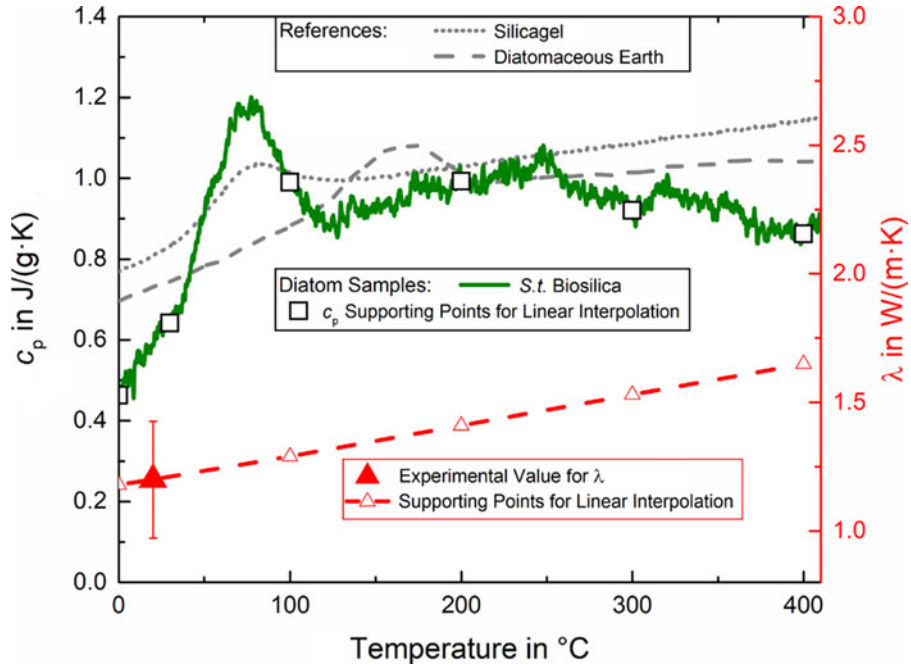

Fig. 3. Temperature dependency of the specific heat capacity c_p and of the thermal conductivity λ of several silica materials.

of approximately 1 µm in diameter. At a distance of about 3.5 µm from the beam spot, the temperature is about 150 K lower. More distant parts of the frustule heat up by about 50 K, while the contact area of the silica with the aluminum sample carrier remains almost at room temperature. The resulting temperature gradient should cause greater mechanical stress to the structure compared to a uniform warming as undergone during the calcination process. At the low scanning speed for imaging, the temperature equilibrium should also be achieved. In contrast, at the higher scanning speed during area scan for CL measurements, the temperature of the diatoms is only increased by about 100 K.

After the prolonged irradiation of the frustules by the electron beam, the EBSD technique was applied to check whether crystallization of the structure was induced by the heat energy input. Since no Kikuchi pattern could be observed, it is concluded that the biosilica retains its amorphous structure. This is in accordance with former studies reporting crystallization at temperatures of 800°C (Arasuna & Okuno, 2018).

EDX Studies of the Eu(III) Distribution

To determine the localization of sorbed Eu(III) on the diatom, elemental distribution images were taken on a typical diatom valve using the Esprit software. The secondary electron image of the diatom (Fig. 5a) is superimposed with the elemental composition map (Fig. 5b).

To excite the characteristic Eu L-lines at about 6 keV photon energies with high probability, element mapping was performed at an acceleration voltage of 13 keV in object region 1 (area scan). With an acquisition time of several hours, the EDX element mappings are time-consuming. As is evident from the element map, Eu is heterogeneously distributed. While high amounts are present at frustule fragments or as Eu-containing aggregates, no significant Eu signal was detected on the regularly structured frustule surface, where the Eu signal intensity does not exceed the noise.

These results of the element mapping are confirmed by the X-ray spectra shown in Figure 6. A spectrum resulting from an area scan over the entire valve (object 1) is compared to spectra with point-like excitation on the honeycomb structure of the cell wall (object 2) and on a frustule fragment/aggregate (object 3).

The X-ray spectra show no significant Eu signals for objects 1 (area scan) and 2, but a clear Eu L-signal in the spectrum of object 3. This also corresponds to the results of an elemental line scan for Eu over the entire diatom through object 3 with the maximum intensity of the Eu L-line in the vicinity of object 3 clearly beyond the background noise (cf. Supplementary Fig. 3).

Detailed values of the local Eu concentrations are intentionally not specified because the complex morphology of the sample and the low amount or thickness of the analyte render quantitative values imprecise.

CL Studies of the Eu(III) Distribution

The Eu(III)-loaded diatom sorbent was studied by CL spectroscopy. To reliably separate the spectral components of the sorbate, luminescence spectra of commercial Eu(III) salt and pure biosilica were acquired, too. Crystalline europium(III) chloride ($EuCl_3 \cdot 6H_2O$) was chosen as a reference material for Eu(III). Figure 7 shows the resulting CL spectrum of Eu(III) without diatom sorbent. Here, the instrumental broadening function is negligible.

The observed spectral lines correspond to the electronic transitions in Eu(III) that can be stimulated by laser excitation (Mathur et al., 2006). The hypersensitive electrical dipole transition $^5D_0$–$^7F_2$ shows the highest intensity, which correlates with the local symmetry of the Eu(III) ion and the nature of the ligands. In contrast, the intensity of the magnetic dipole transition $^5D_0$–$^7F_1$ is largely independent of the chemical environment. Its intensity in the depicted spectrum is about one-fourth of the intensity of the strongest peak. The intensity of the induced electrical dipole transition $^5D_0$–$^7F_4$, also depending on symmetry and

https://doi.org/10.1017/S1431927621012745 Published online by Cambridge University Press

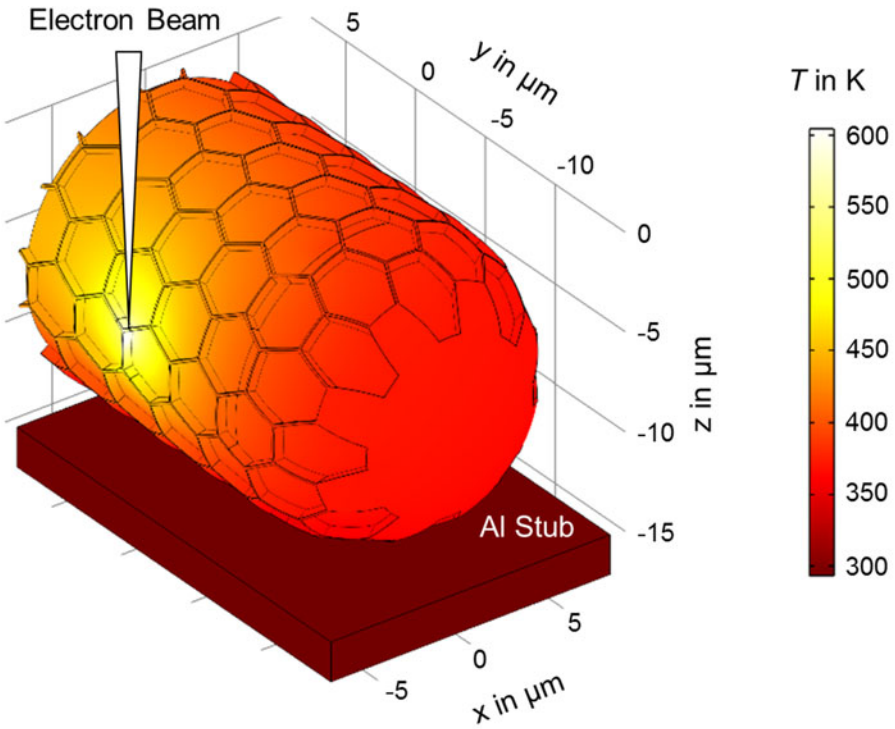

Fig. 4. Equilibrium temperature distribution in a diatom frustule (hollow cylinder with honeycomb-like texture) due to excitation by an idle focused electron beam (white triangle). Temperatures are color-coded as indicated. In order to illustrate the geometry of the diatom, a scaling in *x*-, *y*- and *z*-coordinate direction is provided.

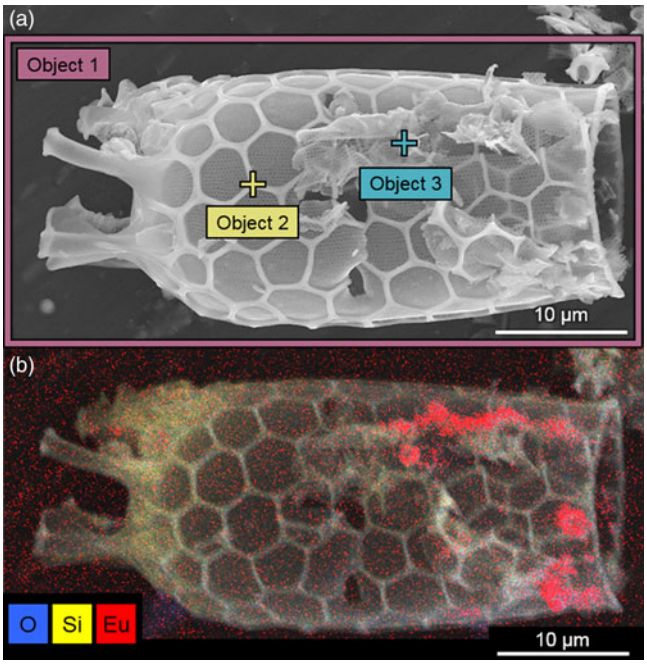

Fig. 5. Diatom valve (*S.t.*) with selected object regions for the element mapping and spectral EDX investigations (**a**). Element mapping with superimposition of the secondary electron image and the local element composition for Si, O, and Eu from EDX mapping (**b**). The Eu L-signal tone was enhanced compared to the Si and O signal for better visibility.

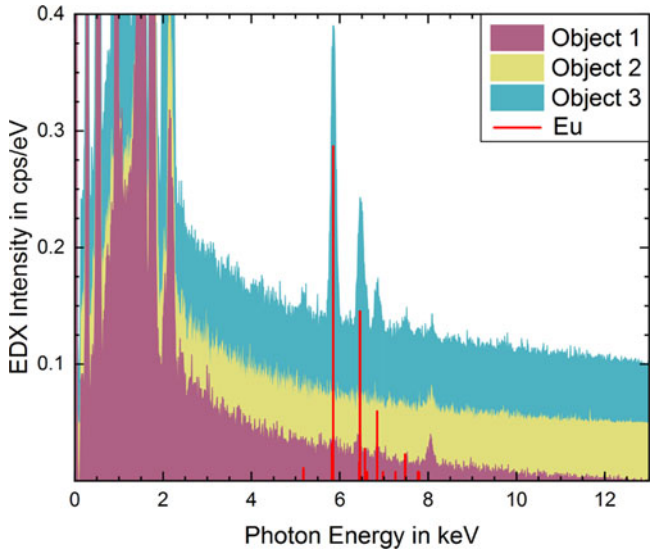

Fig. 6. EDX spectra of objects 1 (area scan), 2, and 3 (point-like excitation) shown in Figure 5a; spectra are shifted by 0.05 cps/eV relative to each other for better distinction. Theoretically expected Eu lines are marked by red lines with intensities according to their probability.

chemical composition, is 1.5 times larger than that of the $^5D_0$–$^7F_1$ transition. As expected, the intensities of the forbidden transitions $^5D_0$–$^7F_0$ and $^5D_0$–$^7F_3$ are very low.

In contrast to the intense, relatively narrow spectral lines of Eu(III), CL spectroscopy on amorphous silica yields broad emission bands of low intensity (Fig. 8). These broad signals result from different native point defect centers in the tetrahedral SiO_2 structure caused by inelastic electron scattering in radiolytic processes (Vigouroux et al., 1985) and the following radiative defect recombination. To gather information about the mean

https://doi.org/10.1017/S1431927621012745 Published online by Cambridge University Press

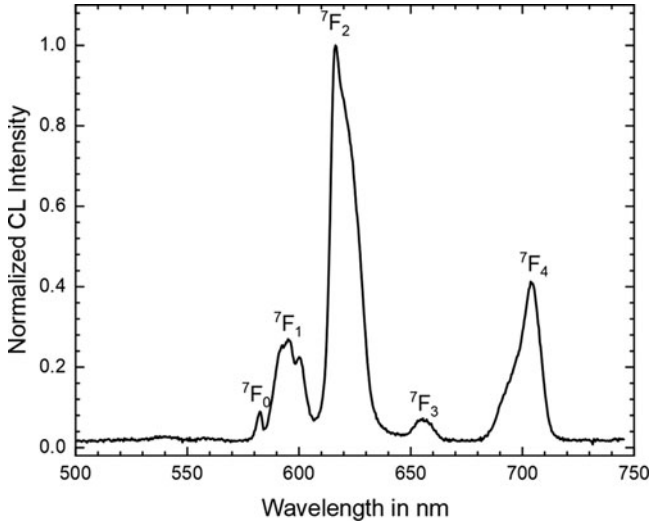

Fig. 7. CL spectrum of $EuCl_3$.

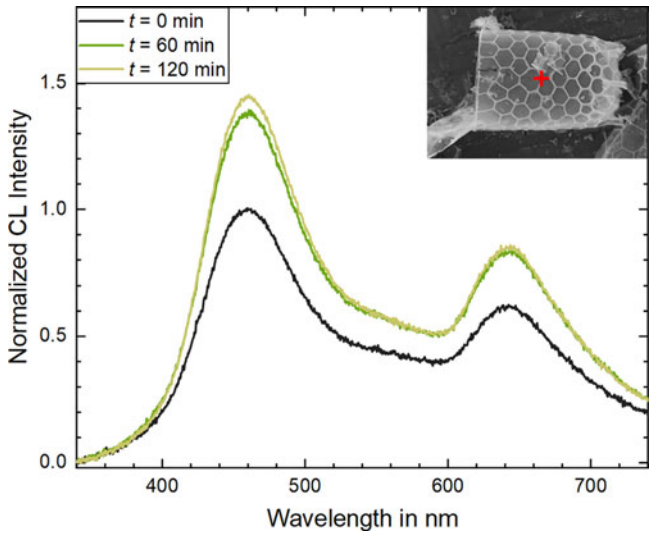

Fig. 8. Exposure time dependency of the CL spectra from a diatom without Eu loading due to point-like excitation on the frustule (red cross in the insert).

and the local luminescence of the biosilica, spectra were recorded during the scanning of the focused electron beam over the entire diatom with a cycle time of 122 ms/frame (cf. Supplementary Fig. 4) and point-like excitation on the frustule (Fig. 8). The shape of the CL spectra depends only slightly on the excitation mode. However, higher intensities are obtained with point-like excitation.

Figure 8 and Supplementary Figure 4 depict that CL spectra depend on the duration of the electron irradiation. The CL spectra were measured immediately at the beginning as well as after 1 and 2 h of exposure time for both excitation modes. The intensity distribution of the emission spectra changes with the duration of the electron irradiation. The width and position of the broad emission bands do apparently not change during the observed exposition time, but the total intensity is rising. A similar result was found for anhydrous fused quartz by Stevens-Kalceff (2013).

Fitting the detected CL spectra by Gaussian-like functions in an eV scale, the two intense peaks and a third, low-intensity signal

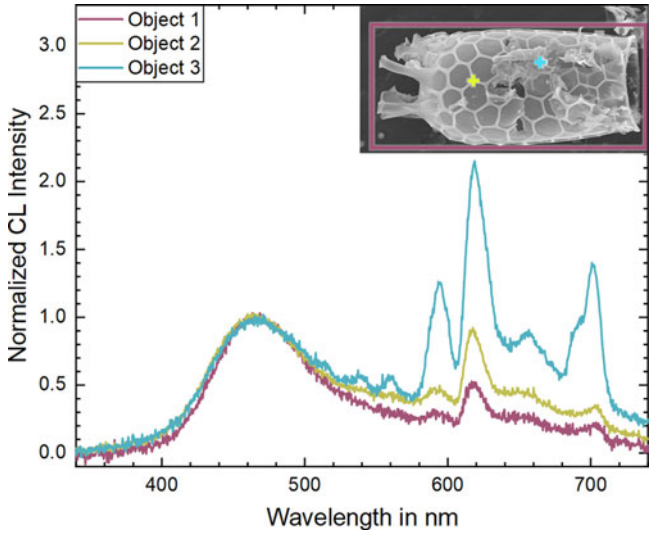

Fig. 9. CL spectra from the Eu diatom sorbate at the beginning of electron irradiation and normalized to the intensity of the peak at 460 nm: excitation on the whole valve (area scan) in violet (window in the insert), point-like excitation on the honeycomb structure in green (cross in the insert), and point-like excitation on the frustule fragment/precipitate in blue (cross in the insert).

in-between (at ca. 560 nm; 2.2 eV) must be considered. In photoluminescence investigations of amorphous α-SiO_2 (Nishikawa et al., 1992; Fitting et al., 2007), the spectral component at ca. 650 nm (1.9 eV) was assigned to non-bridging oxygen hole centers. The component at ca. 560 nm (2.2 eV) is due to the radiative recombination of self-trapped excitons. The signal at 2.7 eV (ca. 460 nm) may originate from oxygen-deficient centers. In the observed range of visible light, the CL spectra obtained from amorphous biosilica closely correspond to the results on pure, synthetic SiO_2 polymorphs. Thus, the emission spectra of both synthetic silica and diatom biosilica are probably caused by similar mechanisms. The increase of the CL intensity with the exposure time as well as for point-like excitation indicates an increasing generation and recombination rate of the produced point defects, which can be thermally assisted.

CL spectra of the Eu-loaded biosilica for different excitation modes are compared in Figure 9 (for time dependency, see Supplementary Fig. 5). As mentioned above, the CL measurements were performed prior to the EDX investigations to minimize the shape change of the frustules increasing with irradiation duration. Apparently, the CL spectra exhibit an additive superposition of the broad bands of the amorphous biosilica and the spectral lines of Eu(III). To eliminate the influence of the irradiation time on the spectra and to illustrate the different local magnitudes of the Eu(III) signal, the CL intensity in Figure 9 was normalized to the intensity of the peak at 460 nm stemming only from the biosilica. The radiative electronic transitions in Eu(III) are clearly visible even in the spectra recorded with an electron beam scanning over the entire surface of the diatom valve. This is a remarkable observation because EDX was not able to detect Eu in this excitation mode. Obviously, CL provides a higher sensitivity and is thus better suited than EDX for studying the Eu distribution. With point-like excitation on the frustule, the spectral lines of the Eu(III) ion are more pronounced. As expected, Eu(III) bands with the highest intensities are observed after excitation on frustule fragments and/or Eu aggregates like object 3.

https://doi.org/10.1017/S1431927621012745 Published online by Cambridge University Press

In the full spectrum, lines assigned to the electronic transitions $^5D_0$–$^7F_1$, $^5D_0$–$^7F_2$, and $^5D_0$–$^7F_4$ are particularly prominent. The forbidden transition $^5D_0$–$^7F_3$ is also apparent. To measure the low-intensity CL emitted by the less luminescent biosilica and by the low proportion of Eu on the frustule surface, the slits of the monochromator system had to be opened more widely. Therefore, the instrumental broadening of about 9 nm is no longer negligible compared to the physical width of the Eu(III) lines. Thus, details of the shape of spectral lines cannot be determined in CL spectra from the regular frustule.

Remarkably, the intensity ratio of the transitions to $^7F_4$ and $^7F_1$ is again about 1.5 for point-like excitation on the sorbate (Fig. 9), as is the case during the $EuCl_3$ measurements. This ratio does not change with the irradiation time. Contrarily, the intensity ratio of the transitions to $^7F_2$ and $^7F_1$ is about 4 in the beginning and increases up to a factor of 8 after 2 h of irradiation with electrons. For details, see Supplementary Figure 5.

The component of the highest intensity among the Eu spectra shown in Figure 9 resembles the spectrum of $EuCl_3$. In particular, the forbidden transitions to $^7F_0$ and $^7F_3$ occur and the spectral line to $^7F_4$ is asymmetric. That means, object 3 in Figure 5a is likely an Eu-containing precipitate.

Conclusions

The amorphous structure and chemical composition of diatom biosilica are proven to be sufficiently stable for the performed measurements in the SEM, which can last for several hours. However, some shape changes of the frustule may occur. Simulations of the temperature distribution within and around the interaction volume of the primary electrons in biosilica suggest that the observed deformations of diatom valves under electron irradiation are probably the effect of thermally driven stress gradients. The energy input of the electron beam may locally heat the biosilica to approximately 300°C. At this temperature, the modification of the frustule shape should neither be caused by mass loss nor by transformation from the amorphous to the crystalline phase of SiO_2 according to the DTA/TG-MS and EBSD investigations.

For the verification of Eu by EDX analysis, the use of the characteristic L-lines of Eu is advantageous, which are not overlaid by the X-ray lines originating from the biosilica. Because a significant Eu signal can only be observed in sample regions with increased Eu concentrations, e.g. in small fragments of diatoms or Eu aggregates/precipitates, EDX investigations are not appropriate to prove the Eu sorption on the overall surface of the diatoms.

As expected, electron energies of 10 keV can be used in the SEM to excite both the radiative transitions of the *f*-electrons in Eu(III) as well as the broad emission bands in biosilica, which can be assigned to known radiative recombination processes. However, the novel results of CL investigations on Eu-loaded biosilica show characteristic Eu(III) spectral lines overlapping with the biosilica CL spectrum. Remarkably, the CL spectral lines of Eu(III) also appear very prominent in frustule regions where EDX spectra do not exhibit significant Eu signals. On the one hand, this demonstrates the higher sensitivity of the CL method for Eu detection. On the other hand, an Eu(III) distribution on the whole surface of the diatom frustules can be determined. Unfortunately, monochromatic CL images are not suitable to visualize the local distribution of Eu(III) on the diatoms due to the additive superposition of the luminescence peaks in the red range of visible light from diatoms and Eu(III).

In future experiments, time-resolved CL measurements could provide further information on the ligand environment of Eu(III) at the biosilica materials. Due to the different excitation processes, deviations from time-resolved photoluminescence signals should become apparent.

Supplementary material. To view supplementary material for this article, please visit https://doi.org/10.1017/S1431927621012745.

Acknowledgments. Financial support from the German BMBF (Federal Ministry of Education and Research) within the FENABIUM project (02NUK046A) is gratefully acknowledged. Special thanks are due to Andrea Brünner and Mai Lê Anh for assistance in sample preparation for SEM and thermal analyses (both Chair of Inorganic Chemistry II, TU Dresden).

References

Alexandre LJT, Pereira MFC, Mauricio AM & Martins-Dias S (2015). Metal spatial distribution assessment in *Phragmites sp.* treating pyrite mining acid drainage: X-ray Micro-CT, SEM-EDS and ICP-AES study. *Microsc Microanal* **21**, 52–53.

Ansone L, Klavins M, Jankevica M & Viksna A (2014). Biomass sorbents for metalloid removal. *Adsorption* **20**, 275–286.

Arasuna A & Okuno M (2018). Structural change of the frustule of diatom by thermal treatment. *Geosci Lett* **5**, 1–7.

Bhowmick S, Stauffer D, Major R, Warren O & Syed Asif SA (2015). A combined effect of electron beam and stress on plastic flow of amorphous silica microparticles. *Microsc Microanal* **21**, 1015–1016.

Bidle KD & Azam F (1999). Accelerated dissolution of diatom silica by marine bacterial assemblages. *Nature* **397**, 508–512.

Binnemans K (2015). Interpretation of europium(III) spectra. *Coord Chem Rev* **295**, 1–45.

Coenen T & Haegel NM (2017). Cathodoluminescence for the 21st century: Learning more from light. *Appl Phys Rev* **4**, 31103.

Comsol AB (2020). Comsol Multiphysics ®. Available at www.comsol.com.

Demers H, Poirier-Demers N, Couture AR, Joly D, Guilmain M, de Jonge N & Drouin D (2011). Three-dimensional electron microscopy simulation with the CASINO Monte Carlo software. *Scanning* **33**, 135–146.

Drouin D, Couture AR, Joly D, Tastet X, Aimez V & Gauvin R (2007). CASINO v2.42—A fast and easy-to-use modeling tool for scanning electron microscopy and microanalysis users. *Scanning* **29**, 92–101.

Fitting H-J, Salh R & Kourkoutis LF (2007). Cathodoluminescence of defects, interstitial molecules, and clusters in silica. *Microsc Microanal* **13**, 1378–1379.

Fritz E (2007). Measurement of cation exchange capacity (CEC) of plant cell walls by X-ray microanalysis (EDX) in the transmission electron microscope. *Microsc Microanal* **13**, 233–244.

Fuya W, Huifen Z, Huang F, Guoxi C, Deqiang W & Hongping H (1995). A mineralogical study of diatomite in Leizhou Peninsula. *Chin J Geochem* **14**, 140–151.

Gaft M, Reisfeld R & Panczer G (2005). *Modern Luminescence Spectroscopy of Minerals and Materials*. Berlin, Heidelberg: Springer Berlin Heidelberg.

Götzke L, Schaper G, März J, Kaden P, Huittinen N, Stumpf T, Kammerlander KKK, Brunner E, Hahn P, Mehnert A, Kersting B, Henle T, Lindoy LF, Zanoni G & Weigand JJ (2019). Coordination chemistry of *f*-block metal ions with ligands bearing bio-relevant functional groups. *Coord Chem Rev* **386**, 267–309.

Gutu T, Dong L, Jiao J, Rorrer GL, Chang C-H, Jeffryes C & Tian Q (2005). Characterization of silicon-germanium oxide nanocomposites fabricated by the marine diatom *Nitzschia frustulum*. *Microsc Microanal* **11**, 1958–1959.

Harrison PJ, Waters RE & Taylor FJR (1980). A broad spectrum artificial sea water medium for coastal and open ocean phytoplankton. *J Phycol* **16**, 28–35.

Heraeus (2019). *Quartz Glass for Optics Data and Properties*. Hanau: Heraeus Quarzglas GmbH & Co. KG.

Iler RK (1979). *The Chemistry of Silica. Solubility, Polymerization, Colloid and Surface Properties, and Biochemistry*. New York, Chichester, Brisbane, Toronto, Singapore: John Wiley and Sons.

Imeson D (1982). On the spatial resolution of EDX composition determination. *Ultramicroscopy* **9**, 307–310.

Jiang W, Luo S, Liu P, Deng X, Jing Y, Bai C & Li J (2014). Purification of biosilica from living diatoms by a two-step acid cleaning and baking method. *J Appl Phycol* **26**, 1511–1518.

Kammerlander KKK, Köhler L, Huittinen N, Bok F, Steudtner R, Oschatz C, Vogel M, Stumpf T & Brunner E (2021). Sorption of europium on diatom biosilica as model of a "Green" sorbent for *f*-elements. *Appl Geochem* **126**, 104823.

Kogel JE, Trivedi NC, Barker JM & Krukowski ST (2006). *Industrial Minerals & Rocks: Commodities, Markets, and Uses*, 7th ed. Colorado: Society for Mining, Metallurgy, and Exploration.

Köhler L, Machill S, Werner A, Selzer C, Kaskel S & Brunner E (2017). Are diatoms "green" aluminosilicate synthesis microreactors for future catalyst production? *Molecules* **22**, 2232. doi:10.3390/molecules22122232.

König J, Lopez-Gil A, Cimavilla-Roman P, Rodriguez-Perez MA, Petersen RR, Østergaard MB, Iversen N, Yue Y & Spreitzer M (2020). Synthesis and properties of open- and closed-porous foamed glass with a low density. *Constr Build Mater* **247**, 118574.

Kooistra WHCF, Gersonde R, Medlin LK & Mann DG (2007). The origin and evolution of the diatoms: Their adaptation to a planktonic existence. In *Evolution of Primary Producers in the Sea*, Falkowski PG & Knoll AH (Eds.), pp. 207–249. Burlington, USA: Academic Press.

Lang Y, Del Monte F, Collins L, Rodriguez BJ, Thompson K, Dockery P, Finn DP & Pandit A (2013). Functionalization of the living diatom *Thalassiosira weissflogii* with thiol moieties. *Nat Commun* **4**, 3683. doi:10.1038/ncomms368.

Liu K (2019). Effects of sample size, dry ashing temperature and duration on determination of ash content in algae and other biomass. *Algal Res* **40**, 101486.

Loucaides S, Behrends T & Van Cappellen P (2010). Reactivity of biogenic silica: Surface versus bulk charge density. *Geochim Cosmochim Acta* **74**, 517–530.

Machill S, Köhler L, Ueberlein S, Hedrich R, Kunaschk M, Paasch S, Schulze R & Brunner E (2013). Analytical studies on the incorporation of aluminium in the cell walls of the marine diatom *Stephanopyxis turris*. *BioMetals* **26**, 141–150.

Mann DG (1999). The species concept in diatoms. *Phycologia* **38**, 437–495.

Matheickal JT, Yu Q & Feltham J (1997). Cu(II) binding by *E. radiata* biomaterial. *Environ Technol* **18**, 25–34.

Mathur JN, Thakur P, Dodge CJ, Francis AJ & Choppin GR (2006). Coordination modes in the formation of the ternary Am(III), Cm(III), and Eu(III) complexes with EDTA and NTA: TRLFS, ^{13}C NMR, EXAFS, and thermodynamics of the complexation. *Inorg Chem* **45**, 8026–8035.

Meradi H, Atoui L, Bahloul L, Labiod K & Ismail F (2016). Characterization of diatomite from Sig region (West Algeria) for industrial application. *Manage Environ Qual Int J* **27**, 281–288.

Molodtsov K, Schymura S, Rothe J, Dardenne K & Schmidt M (2019). Sorption of Eu(III) on Eibenstock granite studied by μTRLFS: A novel spatially-resolved luminescence-spectroscopic technique. *Sci Rep* **9**, 6287.

Nawrocki J (1997). The silanol group and its role in liquid chromatography. *J Chromatogr A* **779**, 29–71.

Nishikawa H, Shiroyama T, Nakamura R, Ohki Y, Nagasawa K & Hama Y (1992). Photoluminescence from defect centers in high-purity silica glasses observed under 7.9-eV excitation. *Phys Rev B* **45**, 586–591.

Nordén M, Albinsson Y, Ephraim JH & Allard B (1992). A comparative study of europium, thorium and uranium binding to an aquatic fulvic acid. *MRS Proc* **294**, 759.

Nowak AP, Sprynskyy M, Brzozowska W & Lisowska-Oleksiak A (2019). Electrochemical behavior of a composite material containing 3D-structured diatom biosilica. *Algal Res* **41**, 101538.

Pohlmann C, Hutsch T, Röntzsch L, Weißgärber T & Kieback B (2013). Novel approach for thermal diffusivity measurements in inert atmosphere using the flash method. *J Therm Anal Calorim* **114**, 629–634.

Prigozhin MB, Maurer PC, Courtis AM, Liu N, Wisser MD, Siefe C, Tian B, Chan E, Song G, Fischer S, Aloni S, Ogletree DF, Barnard ES, Joubert LM, Rao J, Alivisatos AP, Macfarlane RM, Cohen BE, Cui Y, Dionne JA & Chu S (2019). Bright sub-20-nm cathodoluminescent nanoprobes for electron microscopy. *Nat Nanotechnol* **14**, 420–425.

Pytlik N, Kaden J, Finger M, Naumann J, Wanke S, Machill S & Brunner E (2017). Biological synthesis of gold nanoparticles by the diatom *Stephanopyxis turris* and in vivo SERS analyses. *Algal Res* **28**, 9–15.

Round EF, Crawford RM & Mann DG (1990). *Diatoms: Biology and Morphology of the Genera*. Cambridge: Cambridge University Press.

Saager S (2016). Electron beam crystallization of amorphous silicon thin films. In *Proceedings of the 2016 Comsol Conference Munich*. Munich: Comsol.

Santos-Beltran M, Paraguay-Delgado F, Garcia-Alamilla R, Santos-Beltran A & Gallegos-Orozco V (2018). In situ XRD study of MoO_3 particles during heat treatment and their capacity of removing the MB. *Microsc Microanal* **24**, 1764–1765.

Stevens-Kalceff MA (2013). Cathodoluminescence microanalysis of silica and amorphized quartz. *Mineral Petrol* **107**, 455–469.

Stumpf T, Curtius H, Walther C, Dardenne K, Ufer K & Fanghänel T (2007). Incorporation of Eu(III) into hydrotalcite: A TRLFS and EXAFS study. *Environ Sci Technol* **49**, 3186–3191.

Tesson B, Genet MJ, Fernandez V, Degand S, Rouxhet PG & Martin-Jézéquel V (2009). Surface chemical composition of diatoms. *ChemBioChem* **10**, 2011–2024.

Vigouroux JP, Duraud JP, Le Moel A, Le Gressus C & Griscom DL (1985). Electron trapping in amorphous SiO_2 studied by charge buildup under electron bombardment. *J Appl Phys* **57**, 5139–5144.

Wang Y, Lu Y, Chen R, Ma L, Jiang Y & Wang H (2014). Lead ions sorption from waste solution using aluminum hydroxide modified diatomite. *J Environ Prot* **5**, 8.

Xiao F & Howard Huang J-C (2009). Comparison of biosorbents with inorganic sorbents for removing copper(II) from aqueous solutions. *J Environ Manage* **90**, 3105–3109.

Yacobi BG & Holt DB (1990). *Cathodoluminescence Microscopy of Inorganic Solids*. New York: Springer.

Yamamoto Y, Takahashi Y & Shimizu H (2010). Systematic change in relative stabilities of REE-humic complexes at various metal loading levels. *Geochem J* **44**, 39–63.

Yuan P, He HP, Wu DQ, Wang DQ & Chen LJ (2004). Characterization of diatomaceous silica by Raman spectroscopy. *Spectrochim Acta A Mol Biomol Spectrosc* **60**, 2941–2945.